Computational and experimental study of solid phase formation during the decompression of high pressure CO_2 pipelines

Sergey Martynov[a], Wentian Zheng[a], Haroun Mahgerefeth[a], Solomon Brown[a,†], Jerome Hebrard[b], Didier Jamois[b], and Christophe Proust[b]

[a] Department of Chemical Engineering, University College London, WC1E 7JE, London, U.K.

[b] INERIS, Accidental Risk Division, Parc Technologique ALATA, BP 2, 60550 Verneuil-en-Hallate, France

[†]Present address: Department of Chemical and Biological Engineering, University of Sheffield, Sheffield S1 3JD, U.K

Abstract

Decompression of CO_2 pipelines is studied both experimentally and numerically to provide a partially validated model as the basis for the prediction of the hazards associated with CO_2 solid formation. The pipeline decompression experiments, performed using a fully instrumented 36.7 m long and 50 mm internal diameter test pipe up to a maximum pressure of 45 bar, incorporating discharge orifice diameters of 4 and 6 mm, reveal the stabilisation of pressure and temperature near the CO_2 triple point. Also, video recordings of the decompression flow in the reinforced transparent section of the steel pipe show that initial stratification of the constituent liquid and vapour phases is followed by rapid CO_2 solid formation and accumulation in the pipe.

To aid the prediction of hazards associated with solids formation in pipelines, a homogeneous equilibrium pipeline decompression model is developed accounting for the pertinent physical properties of CO_2 in the liquid, vapour and solid states. The model is validated against the experimental data, showing ability to accurately predict the measured pressure and

temperature variations with time along the pipe, as well as the time and amount of the solid CO_2 formed upon decompression across the triple point.

Keywords

CO_2 hazards, solid CO_2, triple point, pipeline decompression, HEM, stratified flow

1. Introduction

Carbon dioxide (CO_2) is emitted in huge quantities in the manufacturing industry and from combustion of fossil fuels in power plants, contributing significantly to global warming. In order to reduce its impact, alongside renewable energy sources, Carbon Capture and Sequestration (CCS) involving capturing the CO_2 and transporting it, most commonly using high-pressure pipelines for subsequent long-term geological storage[1,2] is widely recognised as the most effective option. However, given that CO_2 is considered an asphyxiant at high concentrations (*ca.* > 7% v/v[3]), the high transportation pressures (typically above 70 bar for dense-phase CO_2) and the enormous quantities involved, the safe operation of CO_2 transportation pipelines is of paramount importance.

One possible cause of failure of high-pressure CO_2 transportation facilities is associated with blockage of pressure relief or blowdown valves by solid CO_2 formed as a result of the near-isentropic decompression to pressures below the CO_2 triple point (5.18 bar[4,5]). Also, the accumulation of solid CO_2 may increase the risk of flow blockage and overfilling of the facility at later stages of operation [6–10].

Central to the corresponding risk mitigation and hence, ensuring the safe design of the transportation facilities, is the understanding of the process of CO_2 depressurisation across the triple point. This has been studied using both experimental techniques and mathematical modelling methods[11–13]. For the former, examples include pipeline blowdown tests performed in several research projects, such as CO2PIPETRANS[14], COOLTRANS[15], and CO2PipeHaz[16]. While these studies primarily focused on the CO_2 release and the subsequent atmospheric dispersion, in the CO2PipeHaz project, for the first time, the direct visual observation of the in-pipe multiphase flow behaviour during decompression was made using a specially constructed transparent section of the pipe[17]. Other experimental campaigns have

indicated a temporary reduction in the rate of decompression near the triple point[11,18,19], although the corresponding CO_2 solid phase formation on crossing its triple point has not been quantified. As such, to the best of our knowledge, no direct experimental observations or measurements of CO_2 solids formed in during the pipeline decompression process have been reported in the open literature.

In order to estimate the amount of solid phase that may form upon rapid decompression of CO_2, a thermodynamic approach can be applied. Although being attractive given its simplicity, such an approach is based on quasi-static process assumption. Hence, it cannot deal with the effects of spatial variations of flow along with fluid/wall heat transfer and friction interactions. Thus, important information, such as the time and location at which CO_2 solids form along the pipeline during the decompression process, is not obtained.

To deal with this, computational fluid dynamics methods have been applied for the analysis of failure consequences of CO_2 transmission pipelines and storage tanks[20,21]. In our previous study, we applied a vessel blowdown model to simulate the CO_2 pipeline puncture release experiments performed as part of the CO2PipeHaz project[22]. The use of vessel blowdown model was justified given that in the case of puncture failure of a relatively short pipeline (233 mm internal diameter and 256 m long), the fluid inertia plays an insignificant role in the decompression process[23]. In a further study[24] to enable the simulation of the CO_2 decompression to pressures below the triple point, we applied an extended Peng-Robinson equation of state to deal with solid phase CO_2. However, due to the underlying zero-dimensional approximation employed in this model, it could not resolve the spatial distribution of CO_2 solid formed along the decompressing pipe.

To address the above, we have employed a one-dimensional Homogeneous Equilibrium Mixture (HEM) pipe flow model (see, e.g.,[25,26]), based on the thermal and mechanical

equilibrium assumption between the constituent phases, to simulate CO_2 pipeline decompression, successfully validating its predictions of the transient pressure and temperature against measurements obtained in a real CO_2 pipeline Full Bore Rupture (FBR) test[25]. The extent of CO_2 solid formation as a function of time and distance along the pipeline was also simulated but not compared against real data that was not obtained in the FBR test. At the time of the FBR experiment, the pipeline was not equipped with a transparent section or any other suitable instrumentation to measure the amounts of solid CO_2 formed in the pipeline during its decompression.

The HEM assumption is applicable for pipeline FBR decompression scenario[17] given the relatively large surface area available for phase disengagement as well as the very large fluid velocities resulting in a fully dispersed flow. However, as indicated by the video recordings of the CO_2 flow in the transparent section of the pipe in the CO2PipeHaz project[17], the vapour and liquid phases became highly stratified during pipeline puncture decompression. Given that pipe puncture failures are statistically far more frequent than FBR [27], the above raises the fundamentally important question as to the extent of the applicability of the HEM assumption in the case of pipeline punctures. This is also relevant given the risk of pressure relief valve blockage during the uncontrolled blowdown of CO_2 pipelines.

This paper presents the development and validation of a CFD model for quantifying the amount of solid phase that may formed during the decompression of CO_2 pipelines. The work is organised as follows. Section 2 summarises the key features of the CFD pipe flow model. Section 3 describes the experimental setup constructed for performing the CO_2 pipeline decompression tests. Section 4 deals with the validation of the CFD model based on comparison of its predictions against the corresponding measurements taken during the

pipeline decompression tests. Section 5 covers conclusions and recommendations for future work.

2. Mathematical modelling

2.1 Pipeline decompression model

To describe the pipeline decompression process, a quasi-one-dimensional model based on the HEM approach assuming thermal and mechanical equilibrium between the fluid phases is adopted in the present study based on the its previous successful application for prediction of discharge form pipelines transporting hydrocarbons[28,29]. The transient mass, momentum and energy conservation equations for the HEM flow are expressed as [26]:

$$\frac{\partial \boldsymbol{U}}{\partial \mathrm{t}}+\frac{\partial \boldsymbol{F}(\boldsymbol{U})}{\partial x}=\boldsymbol{S} \tag{1}$$

where $\boldsymbol{U}$, $\boldsymbol{F}$ and $\boldsymbol{S}$ are respectively the vectors of the conservative variables, flux functions and source terms, defined as:

$$\boldsymbol{U}=\begin{pmatrix} \rho A \\ \rho u A \\ \left(u^2/2+e\right)\rho A \end{pmatrix},\quad \boldsymbol{F}=\begin{pmatrix} \rho u A \\ (\rho u^2+p)A \\ \left[\rho\left(u^2/2+e\right)+p\right]uA \end{pmatrix},\quad \boldsymbol{S}=\begin{pmatrix} 0 \\ p\dfrac{\partial A}{\partial x}+2f\rho u^2 A/D \\ \left(2f\rho u^3+4q\right)A/D \end{pmatrix} \tag{2}$$

Here p is the pressure, u is the velocity, ρ and e are respectively the mixture density and specific internal energy. D and A are respectively the local diameter and cross-sectional area of the pipeline, while f is the Fanning friction factor, calculated based on the HEM fluid properties using Chen's correlation[30] and q is the heat flux at the pipe wall. Note that both D

and *A* can vary with the distance along the pipe to account for the reduction in the effective flow area at the puncture end (Figure 1).

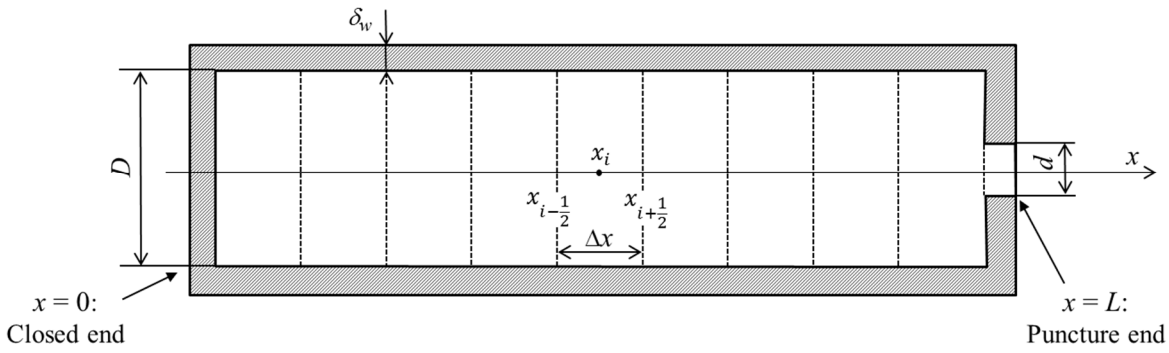

Figure 1. Schematics of an isolated pipe section closed on one side (x=0) and punctured at another end (x=L), main dimensions and the finite volume discretisation.

2.2 Heat transfer

The conjugate problem of heat exchange between the fluid and the pipe wall, is modelled using a set of equations describing the heat transfer in the fluid and heat conduction in the pipe wall. Given high thermal conductivity of the pipe wall, the heat transfer in the wall can be modelled using the lumped thermal capacity model[22]:

$$\rho_w C_{p,w} \delta_w \frac{\partial T_w}{\partial t} = q \tag{4}$$

where ρ_w, $C_{p,w}$ and δ_w are the density, heat capacity and thickness of the pipe wall respectively, and T_w is the local pipe wall temperature.

To calculate the heat transfer to the flow, different correlations are applied depending on the fluid phase composition.

Single-phase flow. In this case, the heat flux, q , is defined using Newton's cooling law:

$$q = htc(T_w - T) \tag{3}$$

where htc is the heat transfer coefficient, determined using the Dittus-Boelter correlation for turbulent forced convection [31].

Liquid-vapour flow. Assuming that nucleate boiling is the dominant mechanism for heat transfer upon rapid flashing of liquid in a pipe [32,33], the heat flux is calculated using Rohsenow's correlation [34]:

$$q = \mu_l h_{lv} \left[\frac{g(\rho_l - \rho_g)}{\sigma} \right]^{0.5} \left[\frac{C_{p,l}(T_w - T)}{0.013 h_{lv} Pr_l} \right]^3$$

where μ, σ, h_{lv}, $C_{p,l}$ and Pr_l are respectively the viscosity, the surface tension, the latent heat of vaporisation, the heat capacity and the Prandtl number of the liquid, calculated using NIST models[35].

Assuming relatively small fractions of solid phase formed upon decompression below the triple point, the single-phase heat transfer model described by equation (3-1) is applied for the solid-vapour mixtures.

2.3 Boundary conditions

In order to close the set of equations (1), boundary conditions are specified at the pipe's intact end and the puncture location (Figure 1).

At the closed end of the pipe the 'solid wall' boundary condition is applied [36]. Here, the velocity is set to zero, while the scalar variables (*i.e.* temperature, pressure and density) are assumed to have zero spatial gradients.

To model the outflow at the puncture end, the variation in the flow area from that of the pipe to the area of the puncture hole is prescribed using an explicit function $A(x)$. This approach enables application of the outflow condition following our previous study[25], where an integral form of a Riemann invariant is applied to express the discharge flow velocity[37]:

$$u_{out} = u_{up} - \int_{p_{up}}^{p_{out}} \frac{dp}{\rho c} \tag{5}$$

where u_{up} is velocity in the flow upstream the release end, while ρ and c are respectively the fluid density and the sound speed at a given pressure and stream entropy.

Equation 5 is first solved together with the sonic condition $u_{out} = c$ to obtain the outflow pressure, p_{out}. If this pressure is higher than the atmospheric pressure, p_a, then the release flow is choked. Otherwise, (*i.e.* $p_{out} < p_a$), the outflow is subsonic and its velocity is obtained by evaluating the integral (5) where p_{out} is set to the ambient pressure.

2.4 Physical properties

Depending on the prevailing fluid pressure and temperature, the fluid can either be single-phase (liquid or vapour), or a two-phase vapour-liquid mixture, or a mixture of vapour, liquid and solid phases at the fluid triple point. To calculate the density and specific internal energy of the HEM fluid in the decompression model equations (1), the following expressions are applied:

$$\rho = \left(\sum_k y_k / \rho_k \right)^{-1}, \; e = \sum_k y_k e_k \tag{6}$$

where y_k is the mass fraction of the k^{th} phase which can be either vapour ($k=v$), liquid ($k=l$) or solid ($k=s$).

The thermodynamic properties of the liquid and vapour phases are calculated using the GERG 2004 equation of state (EoS)[38], while the solid and vapour properties along the sublimation line are predicted using the extended PR EoS[24].

An isentropic speed of sound of the fluid required for the numerical solver (see next section) is defined as:

$$c = \sqrt{\left(\frac{\partial p}{\partial \rho}\right)_s} \tag{7}$$

This definition is applied to define the speed of sound of liquid, vapour and vapour-liquid equilibrium mixtures. However, the above produces a singularity in the speed of sound at the triple point of an HEM fluid, where the sound speed becomes zero, *i.e.* $c = 0$. In order to overcome this singularity, the speed of sound at the triple point is calculated using the following expression for the homogeneous frozen mixture [25]:

$$\frac{1}{\rho c^2} = \sum_{k=v,l,s} \frac{y_k}{\rho_k c_k^2} \tag{8}$$

2.5 Numerical method

In order to numerically solve the flow equations (1), Godunov's finite volume method utilising an approximate Riemann solver and a fractional step technique is applied[36]. For this purpose, the spatial flow domain is subdivided into a finite number of equally-spaced control volumes (Figure 1). The time integration of the flow equations (1) then proceeds in two steps.

In the first step the homogeneous part of equations (1) is explicitly integrated over a control volume $[x_{i-1/2},\ x_{i+1/2}]$ and the time interval $[t_n,\ t_{n+1}]$ to update the vector of conservative variables:

$$\boldsymbol{U}_i^{n+1} = \boldsymbol{U}_i^n + \frac{\Delta t}{\Delta x}\left[\boldsymbol{F}_{i-1/2} - \boldsymbol{F}_{i+1/2}\right] \tag{9}$$

where $\Delta x = x_{i+1/2} - x_{i-1/2}$ is the finite volume width, $i = 1 \ldots i_{\max}$ is the cell index, and $\Delta t = t_{n+1} - t_n$ is the time step satisfying the *CFL* condition:

$$CFL = \frac{\Delta t\left(\left|u \pm c\right|_{\max}\right)}{\Delta x} \le 1 \tag{10}$$

while $\boldsymbol{U}_i$ is the vector of averaged conservative variables in $\left[x_{i-1/2}, x_{i+1/2}\right]$ and $\boldsymbol{F}_{i\pm1/2}$ are Godunov's fluxes defined at the cell interfaces. The latter are calculated using the first-order upwind HLLC approximate Riemann solver [39]:

$$\boldsymbol{F}_{i\pm1/2} = \begin{cases} \boldsymbol{F}_- & , \quad 0 \le S_- \\ \boldsymbol{F}_- + S_-\left(\boldsymbol{U}_-^* - \boldsymbol{U}_-\right), & S_- < 0 < S^* \\ \boldsymbol{F}_+ + S_+\left(\boldsymbol{U}_+^* - \boldsymbol{U}_+\right), & S^* \le 0 < S_+ \\ \boldsymbol{F}_+ & , \quad 0 \ge S_+ \end{cases} \tag{11}$$

where $S_\pm = u \pm c$ are the wave speeds of the corresponding fastest left-going (–) and right-going (+) waves, while $\boldsymbol{U}_\pm^*$ is the vector of conservative variables in the region bounded by the S_+ and S_- waves, and S^* is the speed of contact discontinuity, which are respectively defined as[39]:

$$\boldsymbol{U}_{\pm}^{*}=\rho_{\pm}\left(\frac{S_{\pm}-u_{\pm}}{S_{\pm}-S^{*}}\right)\begin{bmatrix}1\\ S^{*}\\ \dfrac{E_{\pm}}{\rho_{\pm}}+\left(S^{*}-u_{\pm}\right)\left[S^{*}+\dfrac{p_{\pm}}{\rho_{\pm}\left(S_{\pm}-u_{\pm}\right)}\right]\end{bmatrix} \tag{12}$$

$$S^{*}=\frac{p_{+}-p_{-}+\rho_{-}u_{-}(S_{-}-u_{-})-\rho_{+}u_{+}\left(S_{+}-u_{+}\right)}{\rho_{-}(S_{-}-u_{-})-\rho_{+}\left(S_{+}-u_{+}\right)} \tag{13}$$

The adopted first-order scheme, although numerically diffusive, has proven to be robust and accurate for resolving decompression flows in pipelines.

In the second step of the fractional splitting method, the solution obtained in the first step is further advanced accounting for the source term, $\boldsymbol{S}$ [36].

The time integration procedure continues until the flow velocity at the pipe exit reaches zero.

The adopted 1st-order scheme requires using sufficient number of the discretisation cells to achieve accurate solution. Based on a grid dependence study (see the supplementary data) it was found that using 200 discretisation cells guarantees sufficiently accurate resolution of the flow for relevant pipeline decompression scenarios considered in the study.

In order to ensure numerical stability of the solution the CFL criterion was set to 0.5.

3. Experimental setup

Figure s 1 and 2 respectively show a schematic representation and a photograph of the test pipe constructed as part of the CO2PipeHaz project[40] to enable the observation and monitoring of solid CO_2 formation during decompression and the validation of the transient flow model presented above. The horizontal 37.6 m long and 50 mm internal diameter, 5 mm wall thickness insulated mild steel pipe is fitted with a remotely operated release valve and a centerline discharge orifice at one end, and an isolation valve connecting the pipe to a CO_2 feed pump at its other end.

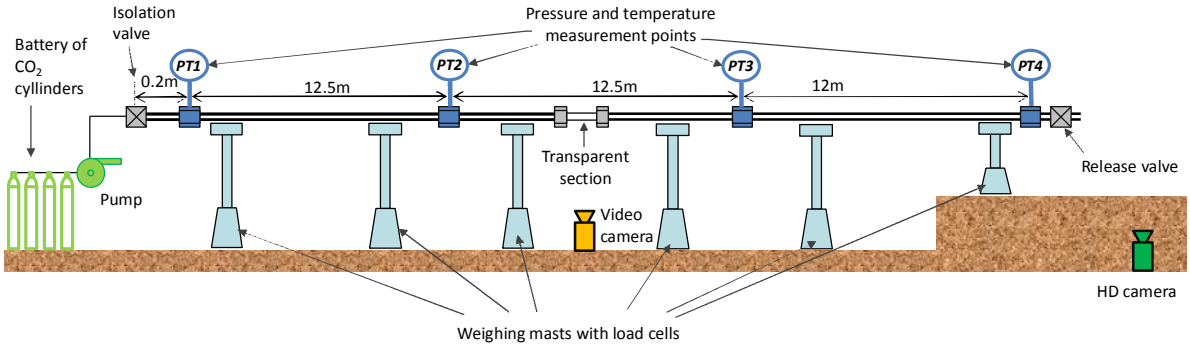

Figure 2. Schematic of the test pipeline equipped with the release device, weighing masts, a transparent section, video cameras and the pressure and temperature measurement locations (*PT1-PT4*).

Figure 3. Photograph of the test pipe.

The fluid pressure and temperature are measured at four instrumentation points, *PT1*, *PT2*, *PT3* and *PT4*, as indicated in Figure 2. The pipe incorporates a pressure sealed reinforced acrylic glass section (0.5 m long, 50 mm i.d. and 15 mm wall thickness) placed at 18.5 m from the feed point to enable video recording of the flow inside the pipe using a high-speed PHOTRON Fastcam APX RS camera. The six pipe supporting masts are fitted with aluminum high-capacity single-point load cells (Tedea-Huntleigh 1250, ± 0.02% accuracy) to enable the measurement of instantaneous pipe weight during the decompression tests. Numerical differentiation of a mean average of the data from the six load cells with respect to time gives the instantaneous discharge flow rate from the pipe.

Figure 4 a shows the pressure and temperature transducers positions around the pipe cross-section at each of the four monitoring locations along the pipe (see Figure 2). Figure 4 b is a photograph of the same arrangement. At each monitoring point, one piezoresistive gauge pressure sensor (Kistler 4622A, 0 – 300 bar, ± 0.05% accuracy) is mounted flush to the internal pipe wall. Three K-type thermocouples (1 mm sleeve Inconel, ± 1.0 ^{o}C error, 1 s response time), are installed to measure the fluid temperature at the top-most (T_H), middle

(T_M) and bottom-most (T_L) locations around the pipe cross-section. The thermocouples measuring T_H and T_L are protruding *ca* 5 mm inside the pipe, while the temperature T_M is measured on the pipe axis. A fourth thermocouple is set flush to the external pipe wall to measure the outer pipe wall temperature, T_w.

(a) (b)

Figure 4. Schematic illustration of the position of pressure and temperature transducers (a) and photograph of the instrumented section of the pipe (b) at one of the four measurement locations.

In order to eliminate safety risks associated with operation of the test facility a detailed analysis of the consequences of the pipe accidental rupturing was performed, including the pipeline overpressure failure, the projection of debris, and the toxic cloud dispersion. On the basis of this study, a safety area with the radius of 40 m was setup surrounding the tests pipe, with no access allowed during the pipeline filling and the rupture tests.

4. Results and discussions

In this section, the pipeline decompression model presented in Section 2 is validated against the measure data from the puncture release experiments performed using the setup described in Section 3.

Table 1 summarises the conditions for the two pipeline decompression tests. The chosen pressure and temperature are relevant to typical nominal operating conditions of pipelines transporting dense-phase CO_2. The orifice diameters have been chosen to be large enough to ensure turbulent flow in the pipe during the decompression, to provide useful data for validation of the pipeline decompression model.

The pipe was purged with dry nitrogen prior to charging with 99.99% purity CO_2 in the sub-cooled liquid state. In the first test, the in-pipe content was discharged through a 6 mm diameter orifice drilled through the centre of a 20 mm flange clamped at the downstream end of the pipe. The second test involved the almost instantaneous opening of an inline ball valve to initiate discharge through a 4 mm downward facing puncture drilled half way along a 1 m long extension pipe securely clamped to the downstream end of the pipe.

Table 1. Conditions of the pipeline decompression tests. Ambient temperature 10 ^{o}C.

Test N°	Orifice diameter (mm)	Orifice location from the feed end (m)	Release direction	Fluid initial conditions		
				p (bar)	T (^{o}C)	Inventory mass (kg)
1	6	37.6	Horizontal	37 ± 0.2	-4 ± 1	70.9 ± 0.18
2	4	38.1	Downward	45 ± 0.2	5 ± 1	67.3 ± 0.18

Figure 5 shows snapshots from the video recordings of the flow through the pipe transparent section taken at 40 s (a), 70 s (b), 340 s (c), 370 s (d), 371 s (e) and 372 s (f) after the initiation of decompression for Test 2 (Table 1). The flow is directed from the left to the right. Arrows on the left of each snapshot indicate the location of the liquid (bottom) /vapour interface (top) which falls as the decompression proceeds. The transition to the solid/vapour mixture (Figure 5 d) on crossing the CO_2 triple point was observed to occur almost instantaneously at 371 s following decompression.

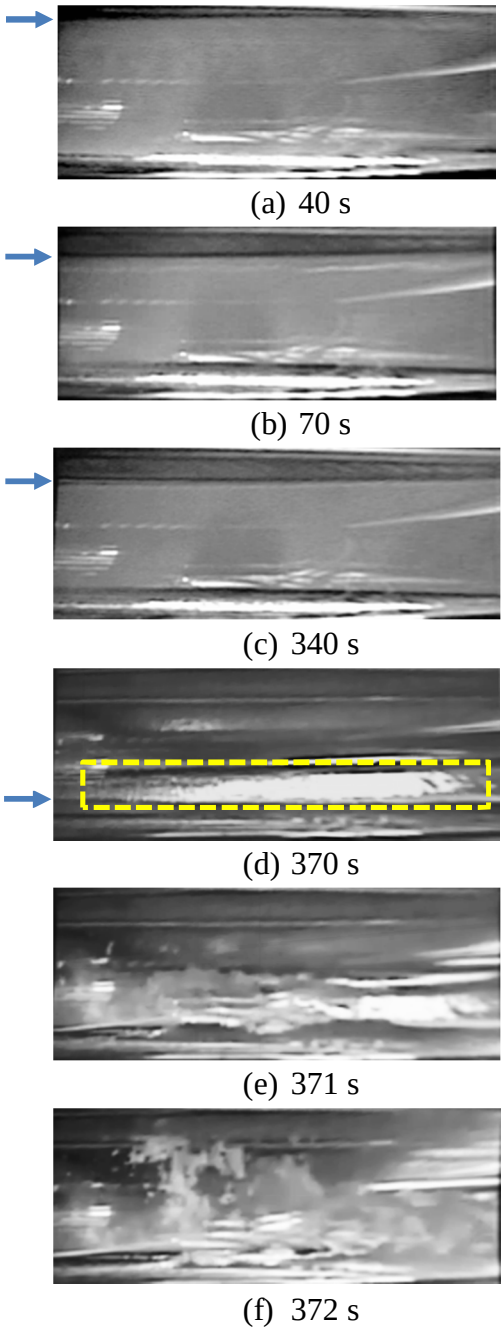

Figure 5. Snapshots from video recordings of the flow in the transparent section of the pipe in Test 2 (Table 1) at different times. The vapour/liquid interface is marked by the arrows.

Figure 6 shows a close-up photograph of the pipe transparent section taken following decompression to 1 bar, showing the extent of solid formation occupying *ca.* 20 % of the pipe volume.

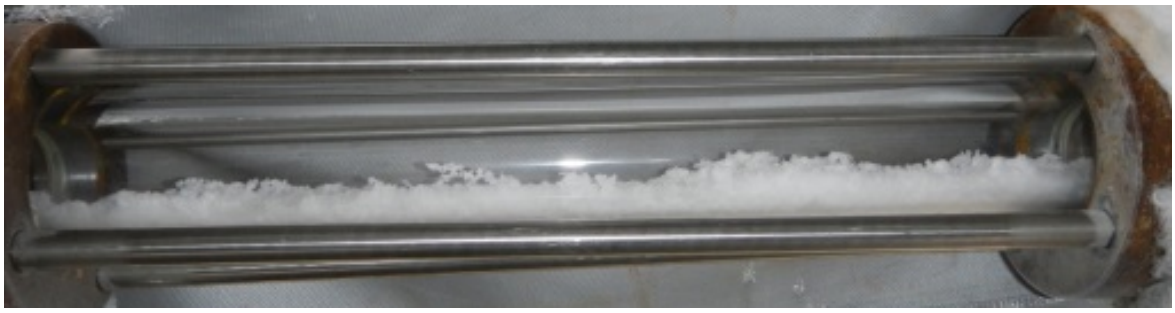

Figure 6. Photograph of the transparent section with solid CO_2 precipitated in the pipe in Test 2 (Table 1).

Figure 7 shows the measured and the simulated variations of pressure with time following decompression for Test 1 and Test 2 recorded at 12.7 m from the pipe closed end (see Figure 2). To ensure convergence and numerical stability, the pipeline was discretised into 200 equally-spaced finite-volume cells (*ca.* 0.2 m/cell) and the *CFL* number (equation 10) was set to 0.5.

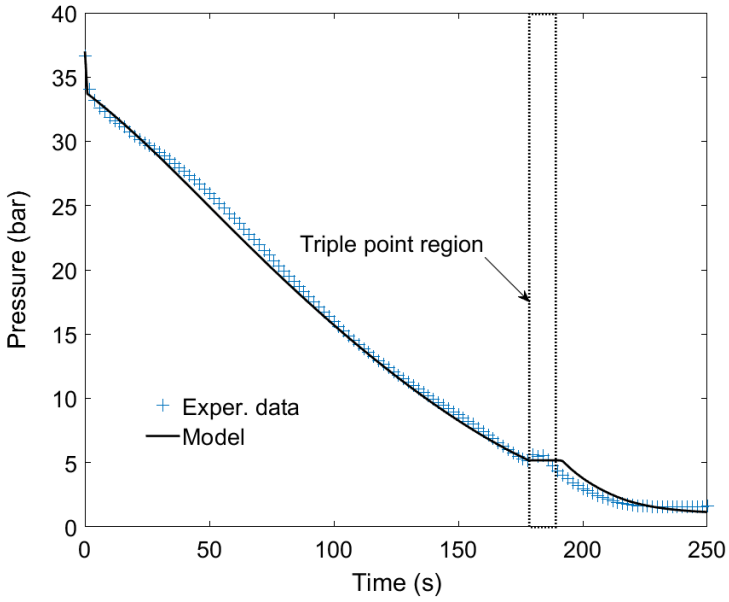

(a)

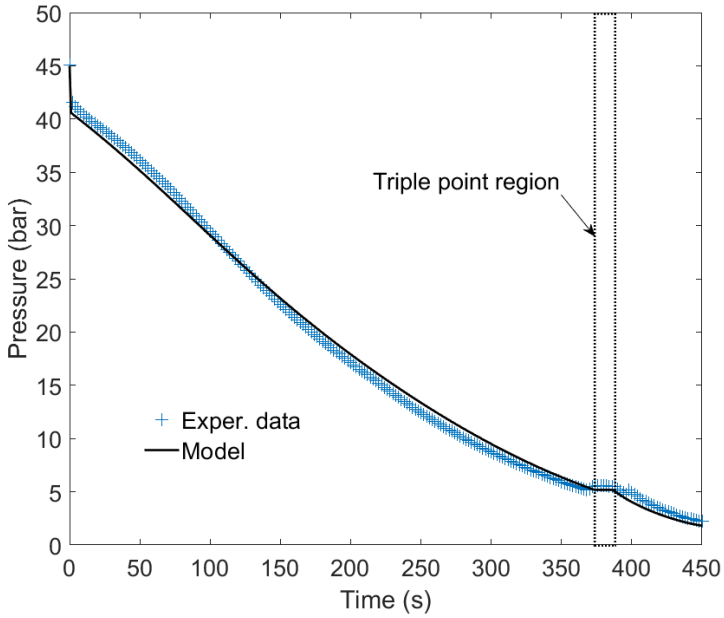

(b)

Figure 7. Predicted and measured pressure variation as a function of time at the second measurement point (Figure 2) in Test 1 (a) and Test 2 (b) (Table 1). Vertical lines mark the time interval when the measured pressure stabilises around the triple point. Pressure is measured to the accuracy of ± 0.2 bar.

The measured pressure *vs* time data show similar trends in both tests (*cf* Figure s 6 a and b), with the simulation results agreeing well with the measurements over the entire duration of release. In particular, at the beginning of the decompression, as a result of the expansion of the nearly incompressible liquid CO_2, the pressure almost instantaneously drops from to the saturation state. This is followed by much slower depressurisation rate corresponding to the liquid evaporation. As expected, given that the discharge orifice diameter employed in Test 1 is 1.5 times larger than for Test 2, the decompression process is considerably faster (*ca.* 2 fold) for the former.

Also, during the latter part of the depressurisation [at *ca.* 180 s in Test 1 (Figure 7 a) and at *ca.* 370 s in Test 2 (Figure 7 b)], the fluid pressure temporarily stabilised near the triple point (5.18 bar) before gradually decreasing to atmospheric pressure. This pressure stabilisation marks the period of time when the flow in the pipe changes its state from the liquid-vapour to solid-vapour mixture at the triple point. The observed good agreement between the model predictions and measurements near the triple point pressure in both tests shows that the model captures well the decompression phenomena across the triple point.

Figure 8 shows the variations of the measured and simulated fluid temperatures at the topmost (T_H) and lowest point (T_L) in the pipe cross-section (see Figure 3) for Tests 1 and 2.

As it may be observed, in both cases, during the first *ca.* 25 s of the release, where the CO_2 remains in the saturated state, the T_H and T_L temperatures coincide.

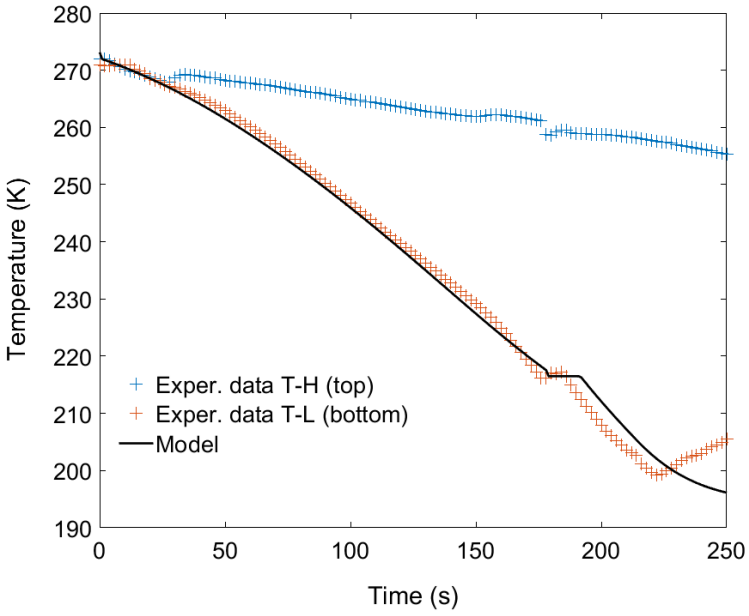

(a)

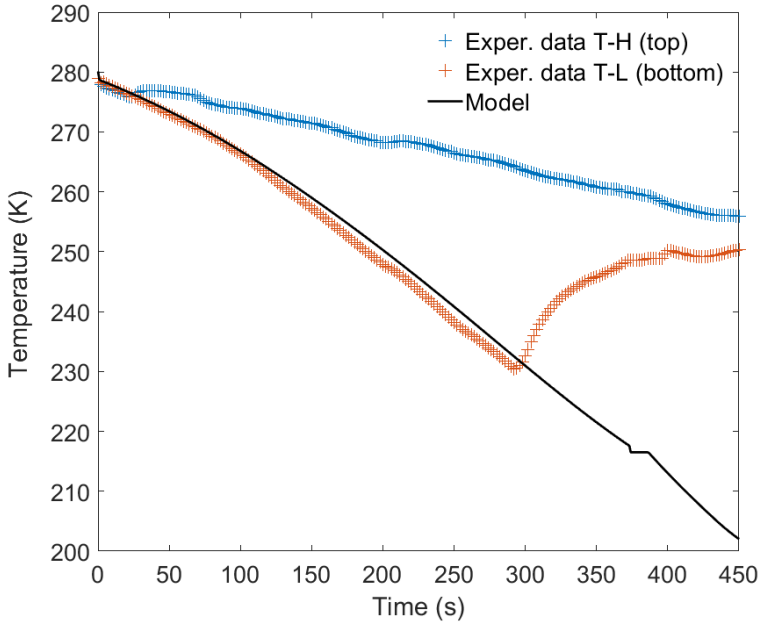

(b)

Figure 8. Time variations of the temperature predicted by HEM model in comparison with the measurements T_H and T_L for Test 1 (a) and Test 2 (b) (Table 1). The temperature is measured with the accuracy ±1 °C.

After *ca.* 40 s, corresponding to the transition from saturated liquid to two-phase flow, the measured liquid temperature, T_L, falls at a significantly faster rate than the vapour temperature, T_H. This departure from thermal equilibrium can be attributed to the effect of stratification of the liquid and vapour phases, as directly observed in the transparent section of the pipe (see Figure 5). The observed higher temperature of the liquid at a given time is because the stratified vapour has a much lower volumetric heat capacity compared to the liquid. This results in the vapour phase absorbing heat from the warmer pipe wall at a faster rate than the liquid phase.

Comparison of the measurements and simulations in Figure 8 shows that in contrast to the vapour temperature (T_H), good agreement between the measured liquid phase temperature, T_L, and the model predictions are obtained during first *ca.* 230 s for Test 1, (Figure 8 a) and 300 s for Test 2 (Figure 8 b). This indicates that during these time domains, despite the observed flow stratification, the HEM assumption produces a reasonably accurate estimation of the liquid phase temperature.

Also, based on Figure 8 a, at *ca*. 180 s, both the measured liquid temperature, T_L and the simulated temperature of the fluid, temporary stabilise near the triple point for about 15 s before dropping again. After *ca.* 230 s, the measured temperature T_L starts to rapidly increase above the saturation temperature predicted by the model. This indicates that at this stage of decompression the thermocouple T_L became exposed to vapour phase, which has much smaller heat capacity than the solid-vapour mixture. In Test 2 (Figure 8b), the departure of T_L from the saturation temperature happens after ca 300 s. This can be attributed to the liquid level falling below the position of the thermocouple T_L, as can be observed in Figure 5 d (albeit at a different location in the pipe and slightly different time).

Figure 9 shows the instantaneous measured and simulated mass of the pipe inventory as a function of time for the two tests (Table 1) during the decompression process.

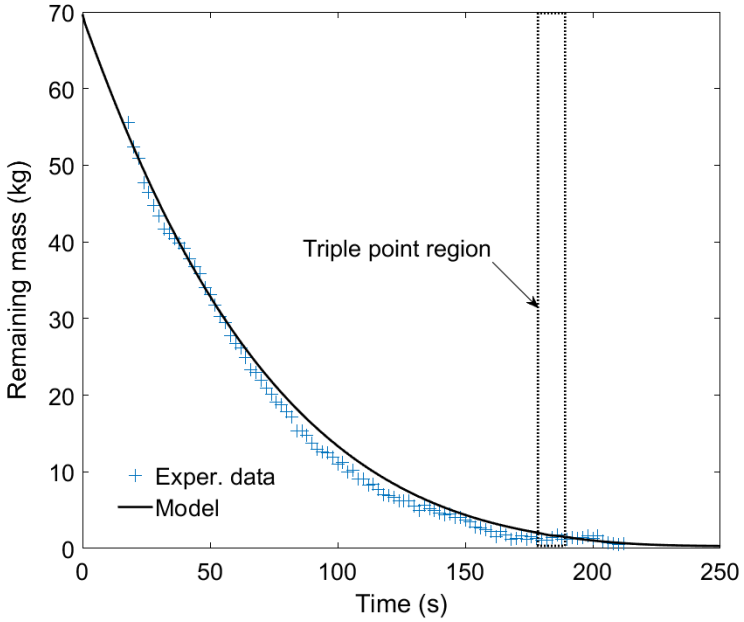

(a)

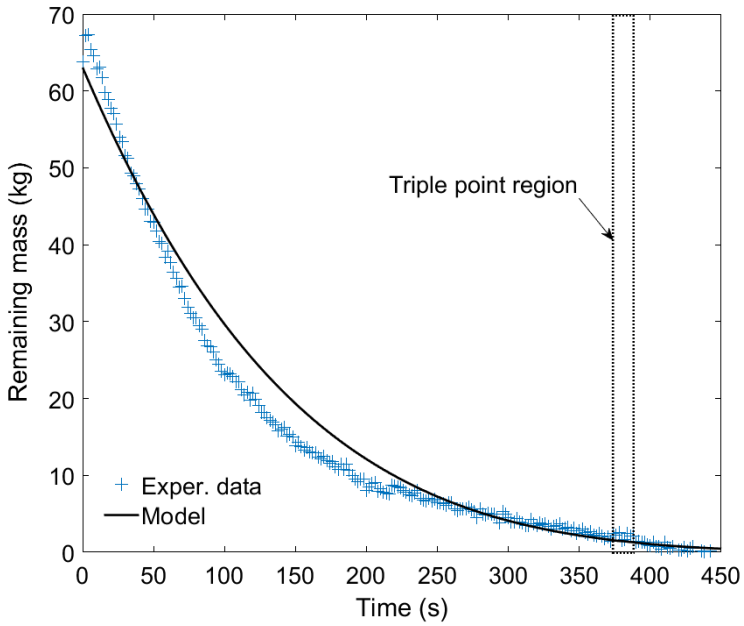

(b)

Figure 9. Predicted and measured remaining inventory as a function of time during decompression for Test 1 (a) and Test 2 (b) (Table 1). Vertical lines mark the time interval

when the measured pressure stabilises around the triple point. The accuracy of the experimental data is ±0.18 kg.

As it may be observed, in both cases, there is relatively good agreement between measured and the simulated data, albeit, Test 1 model predictions compare better the measurements than that for Test 2. This is most likely as a consequence of the CO_2 jet reaction force due to the downward puncture orientation in Test 2 interfering with the load cell measurements.

Table 2 lists the predicted pipe inventory total mass (vapour and solid) and the corresponding solid phase mass fraction data at the triple point using the flow model presented above for both decompression tests. Only the total measured vapour and solid mass data are reported given the practical difficulties in measuring the individual phases. Also included are the corresponding data based on the simplistic conservative assumption of isentropic decompression (the thermodynamic model, see Supporting Information).

Table 2. Amounts of inventory and fractions of solid CO_2 formed in the pipe upon decompression to the triple point pressure.

Test N°	Total mass, *M* (kg)			Solid mass fraction (%)		Solid volume fraction (%)	
	Exp. data	Flow model	Thermodyn. model (Eq. A4)	Flow model	Thermodyn. model (Eq. A2)	Flow model	Thermodyn. model (Eq. A3)
1	1.5±0.18	1.42	2.02	23.3	46.5	0.28	3.46
2	1.8±0.18	1.28	1.93	14.7	43.8	0.16	3.14

As it may be observed, considering the uncertainty in the measurements (±0.18 kg), the flow model produces a reasonably good agreement of the total mass with the measured data, albeit underestimating it for both tests. As expected, the degree of disagreement is higher for Test 2 given the previously discussed downward orientation of the discharge orifice and the corresponding CO_2 jet reaction force. The resulting upward thrust reduces the 'effective' measured mass. The thermodynamic method produces the largest predicted amount of solid given that the finite heat transfer from the pipe wall to the expanding CO_2 is ignored due to the isentropic assumption.

As can be further seen from the data in Table 2, despite its predicted large mass fraction (> 10 %) at the triple point, the significantly higher (*ca.* 100 fold) CO_2 solid phase density as compared to the vapour phase translates into a relatively small (less than *ca*. 0.3%) solid volume fraction. The latter can be compared to the solid volume fraction estimated based on direct visual observations of flow in the transparent section of the pipe shown in Figure 6. As can be seen, the solid formed in the pipe in Test 2 occupies *ca.* 20% of the available space, which is significantly larger than those predicted from the flow model (*ca.* 0.16%, see Table 2) or the thermodynamic model (*ca.* 3.14%, see Table 2). This difference can simply be attributed to the fact that apparent volume of non-compact, porous solid CO_2 settled in the lower part of the pipe cross-section (Figure 6) can be much larger than the actual volume taken by solid phase particles. In practical applications, these highly porous agglomerations of the solid phase may create obstructions to the flow, causing blockage of valves and vent sections in pipelines during rapid decompression. The solids formed in the pipeline, if left untreated, may lead to increased chances of the pipeline material failure due to thermal fatigue and embrittlement, and also the system overfilling and overpressure, potentially leading to accidental rupture. In this respect, taking into account for the solid phase formed during rapid decompression in pipelines will be important when proposing adequate

measures to prevent the solid formation or minimising its disruptive impact on the system efficient and safe operation.

5. Conclusions and future work

In this paper the results of experimental and modelling studies on solid formation during CO_2 pipeline puncture decompression surpassing the CO_2 triple point were presented. The study was initiated in the first instance given the risks associated with the blockage of pressure relief valves by solid CO_2 formed during the uncontrolled blowdown of high-pressure CO_2 transmission pipelines employed as part of the CCS chain. A secondary, but equally important objective was to predict the amount of solid CO_2 released during the accidental puncture of CO_2 pipelines. In these failure scenarios, the ability to accurately provide such data is critically important given that the delayed sublimation and evaporation of the escaping solid CO_2 will dramatically affect the CO_2 hazard profile including the minimum safety distances and emergency response planning. Previous work on the above topic has primarily focused on the more catastrophic but less frequent pipeline FBR failures. Here, the application of the HEM model where the constituent phases are assumed to remain at thermal and mechanical equilibrium during the highly transient discharge process was found to be successful given the observed fully dispersed flow. A further fundamentally important question addressed in this work is the extent of the applicability of the HEM model in predicting the decompression behaviour of CO_2 pipelines during puncture failures.

The experimental part of this study provided detailed measurements of the fluid pressure, temperature and discharge flow rate during depressurisation of sub-cooled liquid CO_2 escaping through different diameter release orifices in the pipe. Visual observation of the flow through the installed transparent section of the pipe and measurements of the fluid temperatures at several locations across the pipe cross-section provided direct experimental

evidence of significant heterogeneous flow. At any given location along the depressurising pipe, the temperature in the liquid phase was found to be as much as 60 ^{o}C lower than that in the vapour phase.

The pipe flow model developed based on the HEM assumption was tested against the measured data, showing good agreement in terms of the pressure and remaining inventory as a function of time during decompression. In particular, the model was able to successfully predict the time at which solid CO_2 was first formed in the pipeline, and also its amount. The predicted CO_2 temperature closely followed the measured liquid phase temperature during the most part of the depressurisation process.

The video recordings of the flow through the transparent section also showed that upon decompression to the triple point pressure, relatively large apparent volumes (*ca.* 20%) of solid phase CO_2 formed inside the pipe. In practice, such occurrence may pose a real risk of pipeline (especially around bends) or pressure relief valve blockage.

It is noteworthy that the solid CO_2 volume predicted based on the flow model was found to be significantly smaller than that observed experimentally. This can be attributed to the homogeneous mixture assumption used in the flow model, which is not capable of resolving accurately the effects of phase separation and agglomeration/ sedimentation of CO_2 solid particles observed in the experiments.

The amount of solid CO_2 was also computed based on thermodynamic relations assuming isentropic decompression process. The results showed that this simple approach is too conservative, significantly overestimating the amount of solid CO_2 formed.

In conclusion, for the ranges of the experimental conditions and failure scenarios tested, the results of this study support the applicability of the simple HEM assumption in providing the

source term for the subsequent risk assessment of the solid CO_2 formed following the puncture failure of pressurised CO_2 pipelines. However, given its inability to predict accurately the temperature of both constituent liquid and vapour phases, the model is not suitable for determining the risk of low temperature induced brittle fracture propagation in multiphase phase CO_2 pipelines. For such risk assessment, the development of a heterogeneous flow model capable of predicting the fluid phase stratification becomes necessary.

6. Acknowledgments

The authors gratefully acknowledge the financial support provided by the European Union 7th Framework Program FP7-ENERGY-2012-1-2STAGE under grant agreement number 309102. The paper reflects only the authors' views and the European Union is not liable for any use that may be made of the information contained therein.

7. Nomenclature

A – flow cross-sectional area,

c – sound speed,

C_p – the heat capacity,

CFL – the Courant-Friedrichs Lewy criterion (eq. 10),

D – pipe diameter,

d – discharge hole diameter,

e – specific internal energy,

f – the Fanning friction factor,

$\boldsymbol{F}$ – vector of flux functions,

htc – heat transfer coefficient,

h_{lv} – the latent heat of vaporisation,

L – pipe length,

M – mass of fluid in the pipeline,

p – pressure,

Pr – the Prandtl number,

q – the heat flux at the pipe wall,

s – entropy,

$\boldsymbol{S}$ – the source term vector,

S – the wave speeds in eq. (13),

t – time,

T – the temperature,

u – velocity,

$\boldsymbol{U}$ – the conservative variables vector,

y_k – the k^{th} phase mass fraction

x – spatial coordinate,

Greek symbols

δ_w – the pipe wall thickness

ρ – density,

μ – coefficient of dynamic viscosity,

σ – surface tension coefficient,

Δt – time step,

Δx – finite volume cell width,

Indices

a – ambient conditions,

i – the finite volume cell index,

k – phase index,

H – the top-most (T_H), middle (T_M) and bottom-most (T_L) locations around the pipe cross-section

l – liquid phase,

L – variables at the left-going wave (eq. 11),

n – the time step index,

o – initial conditions prior to decompression,

out – at the discharge hole

R – variables at the right-going wave (eq. 11),

s – solid phase,*up* – upstream the discharge hole

v – vapour phase,

w – pipe wall

* – the ‘star region’ variables (eq. 11),

8. References

(1) IPCC. *Carbon Dioxide Capture and Storage*; Metz, B., Davidson, O., De Coninck, H., Loos, M., & Meyer, L., Ed.; Cambridge University Press: Cambridge, UK, 2005; Vol. 2.

(2) Styring, P.; Jansen, D.; de Coninck, H.; Reith, H.; Armstrong, K. *Carbon Capture and Utilisation in the Green Economy*; The Centre for Low Carbon Futures and CO2Chem Publishing, 2011.

(3) Harper, P.; Wilday, J.; Bilio, M. *Assessment of the Major Hazard Potential of Carbon Dioxide (CO2)*; 2011.

(4) Huang, D.; Quack, H.; Ding, G. L. Experimental Study of Throttling of Carbon Dioxide Refrigerant to Atmospheric Pressure. *Appl. Therm. Eng.* **2007**, *27*, 1911–1922.

(5) Clayton, W. E.; Griffin, M. L. Catastrophic Failure of a Liquid Carbon Dioxide Storage Vessel. *Process Saf. Prog.* **1994**, *13* (4), 202–209.

(6) DNV. *Design and Operation of CO2 Pipelines. Recommended Practice DNV-RP-J202*; 2010.

(7) Chart Inc. *CO2 Storage Tank - Product Manual*; New Prague, MN 56071 USA, 2014.

(8) Kim-E, M. E. The Possible Consequences of Rapidly Depressurizing a Fluid, Massachusetts Institute of Technology, 1981.

(9) Emerson Climate Technologies. *Commercial CO2 Refrigeration Systems. Guide for Subcritical and Transcritical CO2 Applications*; 2015.

(10) Huang, D.; Ding, G.; Quack, H. New Refrigeration System Using CO2 Vapor-Solid as Refrigerant. *Front. Energy Power Eng. China* **2008**, *2* (4), 494–498.

(11) Munkejord, S. T.; Hammer, M.; Løvseth, S. W. CO2 Transport: Data and Models - A Review. *Appl. Energy* **2016**, *169* (7465), 499–523.

(12) Aursand, P.; Hammer, M.; Munkejord, S. T.; Wilhelmsen. Pipeline Transport of CO2 Mixtures: Models for Transient Simulation. *Int. J. Greenh. Gas Control* **2013**, *15*,

174–185.

(13) Pham, L. H. H. P.; Rusli, R. A Review of Experimental and Modelling Methods for Accidental Release Behaviour of High-Pressurised CO2 Pipelines at Atmospheric Environment. *Process Saf. Environ. Prot.* **2016**, *104*, 48–84.

(14) DNV GL. CO2PIPETRANS project https://www.dnvgl.com/oilgas/joint-industry-projects/ongoing-jips/co2pipetrans.html (accessed Oct 1, 2017).

(15) Barnett, J.; Cooper, R. The COOLTRANS Research Programme: Learning for the Design of CO2 Pipelines. In *ASME. International Pipeline Conference.Volume 1: Design and Construction; Environment; Pipeline Automation and Measurement*; ASME: Calgary, Alberta, Canada, September 29–October 3, 2014, 2014; p 13.

(16) Woolley, R. M.; Fairweather, M.; Wareing, C. J.; Falle, S. A. E. G.; Mahgerefteh, H.; Martynov, S.; Brown, S.; Narasimhamurthy, V. D.; Storvik, I. E.; Sælen, L.; et al. CO2PipeHaz: Quantitative Hazard Assessment for Next Generation CO2 Pipelines. *Energy Procedia* **2014**, *63*, 2510–2529.

(17) Brown, S.; Martynov, S.; Mahgerefteh, H.; Proust, C. A Homogeneous Relaxation Flow Model for the Full Bore Rupture of Dense Phase CO2 Pipelines. *Int. J. Greenh. Gas Control* **2013**, *17*, 349–356.

(18) Brown, S.; Martynov, S.; Mahgerefteh, H. A Coupled Two-Phase Flow Model for Predicting the Flashing of Liquid CO2 during Pipeline Decompression. In *Turbulence, Heat and Mass Transfer 8*; Hanjalic, K., Miyauchi, T., Borello, D., Habziabdic, M., Venturini, P., Eds.; Begell House, Inc: Sarajevo, Bosnia and Herzegovina, 2015; pp 1–12.

(19) Hébrard, J.; Jamois, D.; Proust, C.; Spruijt, M.; Hulsbosch-Dam, C. E. C.; Molag, M.; Messina, E. Medium Scale CO2 Releases. *Energy Procedia* **2016**, *86*, 479–488.

(20) Brown, S.; Martynov, S.; Mahgerefteh, H.; Chen, S.; Zhang, Y. Modelling the Non-Equilibrium Two-Phase Flow during Depressurisation of CO2 Pipelines. *Int. J. Greenh. Gas Control* **2014**, *30*, 9–18.

(21) Mahgerefteh, H.; Brown, S.; Denton, G. Modelling the Impact of Stream Impurities on Ductile Fractures in CO 2 Pipelines. *Chem. Eng. Sci.* **2012**, *74*, 200–210.

(22) Martynov, S.; Brown, S.; Mahgerefteh, H.; Sundara, V.; Chen, S.; Zhang, Y. Modelling Three-Phase Releases of Carbon Dioxide from High-Pressure Pipelines. *Process Safety and Environmental Protection*; Institution of Chemical Engineers, 2014; Vol. 92, pp 36–46.

(23) Mahgerefteh, H.; Jalali, N.; Fernandez, M. When Does a Vessel Become a Pipe? *AIChE J* **2003**, *57* (12), 3305–3314.

(24) Martynov, S.; Brown, S.; Mahgerefteh, H. An Extended Peng-Robinson Equation of State for Carbon Dioxide Solid-Vapor Equilibrium. *Greenh. Gases Sci. Technol.* **2013**, *3* (2), 136–147.

(25) Zheng, W.; Mahgerefteh, H.; Martynov, S.; Brown, S. Modelling of CO2 Decompression across the Triple Point. *Ind. Eng. Chem. Res.* **2017**, *56*, 10491–10499.

(26) Brown, S.; Martynov, S.; Mahgerefteh, H. Simulation of Two-Phase Flow through Ducts with Discontinuous Cross-Section. *Comput. Fluids* **2015**, *120*, 46–56.

(27) Crawley, F. K.; Lines, I. G.; Mather, J. Oil and Gas Pipeline Failure Modelling. *Trans IChemE Part B* **2003**, *81* (3), 3–35.

(28) Oke, A.; Mahgerefteh, H.; Economou, I.; Rykov, Y. A Transient Outflow Model for Pipeline Puncture. *Chem. Eng. Sci.* **2003**, *58*, 4591–4604.

(29) Richardson, S.; Richardson, S.; Saville, G.; Saville, G.; Fisher, S.; Fisher, S.; Meredith, a; Meredith, a; Dix, M.; Dix, M. Experimental Determination of Two-Phase Flow Rates of Hydrocarbons Through Restrictions. *Process Saf. Environ. Prot.* **2006**, *84* (January), 40–53.

(30) Chen, N. H. An Explicit Equation for Friction Factor in Pipe. *Ind. Eng. Chem. Fundam.* **1979**, *18* (3), 296–297.

(31) Dittus, F. W.; Boelter, L. M. K. Heat Transfer in Automobile Radiators of the Tubular Type,. In *University of California publications in engineering*; University of California Press: Berkeley, California, 1930; Vol. 2, p 443.

(32) Mahgerefteh, H.; Wong, S. M. . A Numerical Blowdown Simulation Incorporating Cubic Equations of State. *Comput. Chem. Eng.* **1999**, *23* (9), 1309–1317.

(33) Haque, M. A.; Richardson, S. M.; Saville, G. Blowdown of Pressure Vessels Part I. Computer Model. *Trans IChemE* **1992**, *70*, 3–9.

(34) Incropera, F. P.; De Witt, D. P. *Fundamentals of Heat and Mass Transfer*, 2nd ed.; John Wiley & Sons: New York, 1985.

(35) Lemmon, E. W.; Huber, M. L.; McLinden, M. O. NIST Reference Fluid Thermodynamic and Transport Properties - REFPROP, NIST Standard Reference Database 23. NIST, Applied Chemicals and Materials Division: Gaithersburg 2013.

(36) LeVeque, R. J. Finite Volume Methods for Hyperbolic Problems. *Cambridge Univ. Press* **2002**, *54*, 258.

(37) Munkejord, S. T.; Hammer, M. Depressurization of CO2-Rich Mixtures in Pipes: Two-Phase Flow Modelling and Comparison with Experiments. *Int. J. Greenh. Gas Control* **2015**, *37*, 398–411.

(38) Kunz, O.; Wagner, W. The GERG-2008 Wide-Range Equation of State for Natural Gases and Other Mixtures: An Expansion of GERG-2004. *J. Chem. Eng. Data* **2012**, *57* (11), 3032–3091.

(39) Toro, E. F. The HLL and HLLC Riemann Solvers. In *Riemann Solvers and Numerical Methods for Fluid Dynamics*; 1997; pp 293–311.

(40) Porter, R. T. J.; Mahgerefteh, H.; Brown, S.; Martynov, S.; Collard, A.; Woolley, R. M.; Fairweather, M.; Falle, S. A. E. G.; Wareing, C. J.; Nikolaidis, I. K.; et al. CO2QUEST: An Overview of Aims , Objectives and Main Findings. *Int. J. Greenh. Gas Control* **2016**, *54* (2), 662–681.

Table of Contents (TOC) Graphic